

# Distribution of Circumstellar Disk Masses in the Young Cluster NGC 2024

J. A. Eisner and John M. Carpenter

*California Institute of Technology  
Department of Astronomy MC 105-24  
Pasadena, CA 91125*

jae@astro.caltech.edu, jmc@astro.caltech.edu

## ABSTRACT

We determine the distribution of circumstellar disk masses in the young ( $\sim 0.3$  Myr) cluster NGC 2024 by imaging a  $2'.5 \times 2'.5$  region in  $\lambda 3\text{mm}$  continuum emission to an RMS noise level of  $\sim 0.75 \text{ mJy beam}^{-1}$  with the Owens Valley Millimeter Array. The mosaic encompasses 147 K-band sources as well as the molecular ridge seen previously in dust continuum emission. We detect 10 point-like sources in  $\lambda 3\text{mm}$  continuum emission above the level of  $5\sigma$  within the unit gain region of the mosaic. One of these sources corresponds to the near-IR source IRS 2, an early B-type star. Two other sources are tentatively associated with low-mass near-IR cluster members, and the remaining 7 sources have no K-band counterparts. Assuming the millimeter continuum point sources represent emission from circumstellar disks and/or envelopes, then  $\sim 6\%$  of the total population (infrared and millimeter sources) in the NGC 2024 mosaic has a circumstellar mass in excess of  $\sim 0.06 M_{\odot}$ . We obtain further constraints on the average circumstellar disk mass by considering the mean millimeter continuum flux observed toward a sample of 140 K-band sources that likely have stellar masses  $\lesssim 1 - 2 M_{\odot}$ . While none of these sources are detected individually above the  $3\sigma$  limit of  $\sim 0.035 M_{\odot}$ , the ensemble of sources are detected in the mean at the  $5\sigma$  level with a mean disk mass of  $\sim 0.005 M_{\odot}$ . Compared to the older ( $\sim 2$  Myr) cluster IC 348, NGC 2024 contains a higher frequency of massive disks/envelopes and has a higher mean disk mass by a factor of  $2.5 \pm 1.3$  among K-band sources, suggesting that the mean circumstellar mass is decreasing with cluster age. We also compare the results for the NGC 2024 and IC 348 clusters to those for the lower-density Taurus star forming region. Finally, we compare our detection limits with the minimum mass estimate for the proto-solar nebula, and discuss possible implications for planet formation.

*Subject headings:* Galaxy:Open Clusters and Associations:Individual:Alphanumeric:NGC 2024, Stars:Planetary Systems:Protoplanetary Disks, Stars: Pre-Main-Sequence

## 1. Introduction

In recent years, high resolution millimeter, infrared, and optical images have provided direct evidence for the existence of circumstellar disks on scales of  $\sim 100$ – $1000$  AU around young stars (e.g., Koerner & Sargent 1995; Dutrey et al. 1996; Padgett et al. 1999; O’Dell & Wong 1996). These disks are the likely birth-sites for planets, and determination of the ubiquity, masses, and evolutionary timescales of circumstellar disks will place constraints on the timescales and mechanisms of planet formation.

While direct imaging has provided concrete evidence for a limited number of circumstellar disks, high resolution observations are difficult to obtain for large ensembles of objects. Therefore, indirect tracers of circumstellar disks are commonly utilized to infer disk evolution. The most common tracer is the presence of near-infrared (near-IR) emission in excess of that expected from the stellar photosphere. Indeed, the ubiquity of near-IR excesses around young stars in Taurus (see, e.g., Strom et al. 1989) provided early indications that disks are common around young solar-mass stars. More recently, JHKL photometric surveys of rich clusters spanning a range of ages detected near-IR excesses for at least 50% of solar mass stars at an age of  $\sim 1$  Myr, but for fewer than 10% of stars with ages from 3–10 Myrs (e.g., Haisch et al. 2001).

The main limitation of near-IR surveys is that the excess emission traces only the hot ( $> 1000$  K), inner ( $\sim 0.1$  AU) disk regions around solar-mass stars. Moreover, the emission is usually optically thick. Therefore, near-IR surveys provide no direct constraints on the reservoir of cold dust located at larger radii where planets are expected to form. To study this cooler material, observations at longer wavelengths, in particular millimeter (mm) and sub-millimeter (sub-mm) wavelengths, are necessary. Since the mm and sub-mm emission is optically thin, the observed flux provides a direct measure of mass.

Several investigators have carried out comprehensive single-dish mm and sub-mm continuum surveys toward regions of star formation comprising loose aggregates of stars: Taurus (Beckwith et al. 1990; Osterloh & Beckwith 1995; Motte & André 2001),  $\rho$  Ophiuchi (André & Montmerle 1994; Nuernberger et al. 1998; Motte et al. 1998), Lupus (Nuernberger et al. 1997), Chamaeleon I (Henning et al. 1993), Serpens (Testi & Sargent 1998), and MBM 12 (Itoh et al. 2003; Hogerheijde et al. 2002). About 20%–30% of stars aged  $\sim 1$  Myr appear to possess circum-

stellar disks with masses greater than  $\sim 0.01 M_{\odot}$ , comparable to the minimum mass of the pre-solar nebula (Weidenschilling 1977; Hayashi 1981), and the median disk mass is  $\lesssim 0.004 M_{\odot}$ .

Expanding millimeter continuum surveys to include rich clusters allows the determination of accurate statistics on the frequency and evolution of disk masses as a function of both stellar mass and age. Also, since most stars in the Galaxy form in rich clusters (Lada et al. 1991; Lada et al. 1993; Carpenter 2000), understanding disk formation and evolution in cluster environments is a vital component in our general understanding of how stars and planets form. The main challenge to observing rich clusters at mm-wavelengths is that very high angular resolution is required to resolve individual sources and to distinguish compact disk emission from the more extended emission of the molecular cloud. Single-aperture mm-wavelength telescopes lack sufficient angular resolution, and to date, only two rich clusters have been observed with mm-wavelength interferometers: the Orion Nebula cluster (Mundy et al. 1995; Bally et al. 1998), and IC 348 (Carpenter 2002). These observations have detected *no* massive disks with  $3\sigma$  upper limits ranging from  $\sim 0.025$ – $0.17 M_{\odot}$ .

Here, we present a mm-wavelength interferometric survey of NGC 2024, a young, deeply embedded stellar cluster in the Orion molecular cloud. In addition to improving the statistics on circumstellar disks in clusters, these observations enable a comparison between relatively young (NGC 2024;  $\sim 0.3$  Myr) and old (Orion Nebula cluster and IC 348;  $\sim 1$ – $2$  Myr) clusters, which places constraints on the timescales for disk evolution. In the next section, we describe the NGC 2024 region and discuss the stellar and protostellar populations. The observations and results are presented in §3 and §4, and we derive constraints on the circumstellar disk masses in §5. Finally, we compare the results for NGC 2024 to those for the IC 348, Orion Nebula cluster, and Taurus regions, and discuss the implications for disk evolution in rich clusters.

## 2. The NGC 2024 Cluster

NGC 2024 is a young HII region embedded in the L1630 (Orion B) molecular cloud. Distance estimates to the Orion region range from  $\sim 360$  –  $480$  pc (Anthony-Twarog 1982; Brown et al. 1994, and references therein), and the distance to the stellar group containing NGC 2024 has been estimated to be  $415$  pc based on uvby photometric and Balmer line measurements of 11 B-stars (Anthony-Twarog 1982). We adopt this distance of  $415$  pc.

Grasdalen (1974) originally identified the brightest infrared source in the region, IRS 2, which has a luminosity of  $\sim 10^6 L_{\odot}$  and is a suspected early B-type star. IRS 2 was

subsequently resolved into two sources, IRS 2 and IRS 2b (Jiang et al. 1984). Recently, Bik et al. (2003) estimated a spectral type of  $\sim$ O8 for IRS 2b, and suggested that it is the dominant source of ionizing flux for the HII region.

NGC 2024 also contains a cluster of lower mass stars, originally identified by Barnes (1989). Lada et al. (1991) identified 309 sources with  $m_K < 14$  within the NGC 2024 cluster, and Lada (1999) computed a stellar density of  $\rho \approx 400$  stars  $\text{pc}^{-3}$ . Meyer (1996) obtained J-,H-, and K-band photometry for 233 cluster members. L-band photometry (and new JHK measurements) for 142 of these stars by Haisch et al. (2000) indicates near-IR excess emission for  $\geq 86 \pm 8\%$  of sources. Thus, a large fraction of the NGC 2024 cluster members have at least a small amount ( $\sim 10^{-6} M_\odot$ ) of hot ( $> 1000$  K) associated circumstellar material, presumably distributed in inner circumstellar disks.

The age of the NGC 2024 cluster has been estimated at  $\sim 0.3$ – $0.5$  Myr (Meyer 1996; Ali 1996), using spectroscopic and photometric data to place cluster members in an HR diagram and then inferring the age from pre-main sequence evolutionary tracks by D’Antona & Mazzitelli (1994). For comparison, the same technique yields ages of  $\sim 1$  and  $2$  Myr for the Orion Nebula cluster and IC 348, respectively (Hillenbrand 1997; Luhman et al. 1998; Luhman 1999). While the absolute ages of the three clusters are uncertain due to limitations of the pre-main sequence evolutionary tracks, the relative ages are more secure. To further clarify the relative ages of the three clusters, we re-calculate the ages in a consistent way using published data compiled by Hillenbrand, Meyer & Carpenter (2003). We place cluster members with masses between  $0.1$  and  $1 M_\odot$  on an HR diagram, and infer the ages from the pre-main sequence tracks of D’Antona & Mazzitelli (1997). We compute logarithmic ages (in years) of  $4.2 \pm 0.9$ ,  $5.5 \pm 0.8$ , and  $6.2 \pm 0.7$  for NGC 2024, the Orion Nebula cluster, and IC 348, respectively. The relative youth of NGC 2024 is also supported by the fact that the cluster remains deeply embedded within the molecular cloud, in contrast to both the Orion Nebula cluster and IC 348 where the extinction to the cluster members is substantially less (Hillenbrand 1997; Luhman et al. 1998; Luhman 1999). In the remainder of the discussion, we adopt an age of  $0.3$  Myr for NGC 2024.

Meyer (1996) estimated the masses for NGC 2024 cluster members using near-IR spectroscopy for 19 sources, and a photometric method based on de-reddening sources to the expected locus of T Tauri stars in color-color diagrams for an additional 72 sources. The resulting mass distribution is statistically consistent with a Miller-Scalo IMF. Figure 1 shows a color-magnitude diagram for NGC 2024 (based on data from Meyer 1996). Although near-IR excess emission, age uncertainties, and binarity complicate the interpretation of this diagram, the observed colors and magnitudes are consistent with most stars in NGC 2024 having masses of  $\sim 0.1$ – $1 M_\odot$ . While some sources ( $\sim 10\%$ ) may have sub-stellar masses,

spectroscopic observations are required to confirm this speculation.

We examined the K-band UKIRT image from Meyer (1996), and found 147 point-like sources within the region we observed at OVRO (see §3). We astrometrically calibrated the UKIRT image using the 2MASS Point Source Catalog, and the residuals of the astrometric fit of the UKIRT image are  $0''.1$ . The astrometric uncertainty of the 2MASS coordinates is  $\lesssim 0''.2$ , and thus the positions of the infrared sources are known to within a fraction of the OVRO beam size ( $\sim 2''$ ; see §3).

In addition to the young stellar population traced by near-IR emission, NGC 2024 also contains a population of deeply embedded objects, invisible at near-IR wavelengths, but traced by mm and sub-mm wavelength emission. Several strong, compact  $\lambda 3\text{mm}$  continuum sources, labeled FIR 1-7 (Mezger et al. 1988; Mezger et al. 1992), are detected in the ridge of mm emission that coincides with the prominent dust lane in NGC 2024. While these compact sources were originally interpreted as dense ( $n_{\text{H}} \sim 10^{14} - 10^{15} \text{ m}^{-3}$ ), cold ( $T \sim 15 - 20 \text{ K}$ ) protostellar condensations (Mezger et al. 1988; Mezger et al. 1992), subsequent observations yielded evidence that at least some of the sources are actually embedded protostars or young stellar objects (e.g., Moore et al. 1989; Richer et al. 1989; Chandler & Carlstrom 1996).

### 3. Observations

We mosaicked a  $2'.5 \times 2'.5$  region toward the NGC 2024 cluster in the  $\lambda 3\text{mm}$  continuum with the OVRO millimeter array between January, 2002 and April, 2003. Continuum data were recorded simultaneously in four 1-GHz bandwidth channels centered at 99.46, 97.96, 102.46, and 103.96 GHz. As shown in Figure 2, the mosaic consists of sixteen pointing centers. Five separate array configurations provided baselines between 15 and 483 meters, and the uv coverage of the observations is shown in Figure 3a.

We calibrated the amplitudes and phases of the data with the blazar J0530+135:  $(\alpha, \delta)_{\text{J2000}} = (5^{\text{h}}30^{\text{m}}56^{\text{s}}.4, +13^{\circ}31'55''.2)$ . We estimated the flux for J0530+135 using Neptune and Uranus as primary flux calibrators, and 3C84 and 3C273 as secondary calibrators. Since we obtained data over two separate observing seasons, and since J0530+135 may be variable, we estimated the flux for each season. For observations up to May, 2002, we determined a mean flux of 2.23 Jy, with an RMS dispersion of 0.16 Jy, as computed from observations on 21 separate nights in which both J0530+135 and flux calibrators were observed. For the observations that began in September 2002, we computed a mean flux of 1.97 Jy, with an RMS dispersion of 0.11 Jy, based on observations on 5 nights in which both J0530+135 and flux calibrators were observed. All data reduction and calibration were performed using the

OVRO software package MMA (Scoville et al. 1993).

We mosaicked the sixteen individual pointings into a single image, then deconvolved and CLEANed the mosaic using the MIRIAD package (Sault et al. 1995). We averaged the data using robust weighting (with a robustness parameter of 0.5) in order to obtain a good balance between sensitivity and angular resolution. Based on observations of circumstellar disks in Taurus, which find disk diameters  $\lesssim 300$  AU (Dutrey et al. 1996), we expect that disks in NGC 2024 (at a distance of 415 pc) will have angular scales of  $\lesssim 0''.7$ . In order to directly observe this compact disk emission, which is effectively point-like at the angular resolution of these observations, we resolved out the extended emission in the OVRO mosaic by using only longer-baseline data. Experimenting with different uv spacing cutoffs, we minimized the RMS noise of the map by eliminating all data with uv spacings  $< 20$  k $\lambda$ .

Because NGC 2024 is at low declination, the uv coverage is often sparse in the north-south direction, and thus beam artifacts in the north-south direction may contain up to 50% as much flux as the main beam. Figures 3b and c show the synthesized beams corresponding to the full uv coverage of the mosaic, and only uv spacings  $> 20$  k $\lambda$ , respectively. The FWHM of the core of the beam using all our OVRO data is  $3''.84 \times 3''.22$  at a position angle of  $-28.5^\circ$ , and the FWHM of the beam core for only outer spacings is  $2''.53 \times 2''.13$  at a position angle of  $-44.2^\circ$ .

#### 4. $\lambda 3\text{mm}$ Continuum Emission

The mosaic produced from all of our robust-weighted NGC 2024 data is shown in Figure 4. The unit gain region of the mosaic encompasses a  $2''.5 \times 2''.5$  area, as indicated by the solid contour. We detect the previously known mm sources FIR 2-6 (Mezger et al. 1988) and IRS 2 (Wilson et al. 1995), as well as extended emission from the molecular ridge (e.g., Chandler & Carlstrom 1996). The horizontal emission regions labeled “NCP” and “SCP” in Figure 4 correspond spatially to the free-free emission regions observed in VLA centimeter continuum maps (Crutcher et al. 1986; Gaume et al. 1992).

We calculate the RMS of the image in  $0''.5 \times 0''.5$  sub-regions after removing the strong point source emission using CLEAN. The “intrinsic” RMS noise in the mosaic is  $\sim 0.6$  mJy, calculated for a  $0''.5 \times 0''.5$  region in the northwest corner of the map that is free of any strong emission. Some regions of the image with more extended emission and sidelobe artifacts (which we could not CLEAN adequately) have an RMS as high as  $\sim 3$  mJy, and the mean RMS across the mosaic is 1.3 mJy.

Figure 5 shows the OVRO mosaic produced from data with uv spacings  $> 20$  k $\lambda$ . The

extended emission seen in Figure 4 is mostly resolved out, and the overall sensitivity is significantly improved. Specifically, the RMS sensitivity within a  $0'.5 \times 0'.5$  region in the northwest corner of the mosaic shown in Figure 5 is  $\sim 0.5$  mJy (compared to  $\sim 0.6$  mJy for Figure 4). The local RMS in  $0'.5 \times 0'.5$  sub-regions varies from  $0.5 - 1$  mJy across the image, and the mean RMS for the mosaic is 0.75 mJy. Since Figure 5 represents such a dramatic improvement over Figure 4 in terms of RMS noise and distinctness of the point sources, we will use this outer spacings map in the remainder of the analysis.

In Figure 5, we detect emission above the  $5\sigma$  level (where sigma is determined locally, as described in the preceding paragraphs) from the compact sources FIR 2-6 and IRS 2, as well as several faint new sources. We choose this detection threshold since  $< 0.01$  out of the  $\sim 6,000$  independent pixels within the unit gain contour are expected to have noise spikes above the  $5\sigma$  level (assuming Gaussian noise). Positions, measured fluxes, sizes, and estimated masses (see §5 below) for all of the compact sources are listed in Table 1. Since the extended emission from the NCP and SCP structures is not completely resolved out of Figure 5, no sources observed towards the NCP and SCP are included. Since some of the weaker sources listed in Table 1 may represent peaks of the underlying extended emission or beam artifacts due to imperfect cleaning, rather than true point sources, they should be treated with some caution.

For each source in Table 1, we fit 2-D elliptical Gaussians to the emission to determine fluxes, positions, and sizes. For three weak sources, the Gaussian fits did not converge, and for these we determine the peak flux, and quote the position of the pixel in which the peak flux occurs. From the fitted sizes listed in Table 1, FIR 2, FIR 3, and source #7 appear to be somewhat resolved. Since we expect typical disks in NGC 2024 to be unresolved in the OVRO image (§3), these resolved sources likely represent envelopes, large disks, or other extended structures.

We now restrict our attention to the mm-wavelength fluxes observed towards the known K-band cluster members within the unit gain contour. For these 147 pre-determined pixel positions,  $\sim 0.2$  sources are expected to show emission above the  $3\sigma$  level from Gaussian noise, and we therefore use a  $3\sigma$  detection level of 2.25 mJy for individual K-band sources. We note that for the entire mosaic,  $\sim 10$  pixels within the unit gain contour are expected to show noise spikes above the  $3\sigma$  level, which is why we used a  $5\sigma$  detection limit above.

Figure 6a shows the distribution of mm-wavelength fluxes observed towards K-band sources in NGC 2024. Several K-band sources have corresponding  $\lambda 3\text{mm}$  fluxes above the  $3\sigma$  level. One of these sources is IRS 2, an early-type B star previously detected by several investigators (e.g., Grasdalen 1974; Wilson et al. 1995). Two other detected sources, FIR 2 and 4, correspond roughly with the positions of near-IR cluster members. However, the

peak of the mm emission for FIR 2 is  $\sim 1''.6 \pm 0''.3$  away from the position of the infrared cluster member, and FIR 4 is  $\sim 0''.7 \pm 0''.3$  away from the nearby infrared cluster member. The other source in Figure 6a above the  $3\sigma$  level is part of the NCP extended structure, and the extreme negative source with  $F \sim -4$  mJy is actually tracing a sidelobe artifact. We exclude these sources, as well as the high-mass stars IRS 1 and IRS 2b, in order to examine the distribution of  $\lambda 3\text{mm}$  fluxes observed towards the remaining 140 “typical” low-mass cluster members.

The observed distribution of  $\lambda 3\text{mm}$  fluxes shown in Figure 6a is different from that expected for pure Gaussian noise with a mean of zero and an RMS of 0.75 mJy in that the fluxes are skewed towards positive values. Weighting the observed fluxes by the locally measured RMS of the image, we determine an RMS of the distribution of 0.94 mJy, with a mean of 0.32 mJy, and a standard deviation of the mean of 0.06 mJy. This positive bias is significant since the noise in the OVRO map is consistent with a Gaussian distribution about a mean of zero (see Figure 6b). Specifically, the distribution of fluxes observed towards all pixels within the unit gain contour of the OVRO mosaic (with the strong point sources listed in Table 1 removed using CLEAN) has a mean of  $-7.6 \times 10^{-5}$  mJy and a standard deviation of 0.78 mJy. Comparison of Figures 6a and 6b suggests that the bias in the distribution of fluxes observed towards K-band sources represents real underlying emission.

The positive bias is also illustrated in Figure 7, which shows an “average” image of the 3mm flux observed towards K-band sources, obtained by averaging  $10'' \times 10''$  images centered around each object. The bright point sources listed in Table 1 were removed using CLEAN before shifting and co-adding the images. Figures 6a and 7 both exhibit a positive bias at the  $\sim 5\sigma$  confidence level. Moreover, the FWHM of the emission in Figure 7 is consistent with a point source centered at the mean position of the K-band sources, including negative features that closely resemble the negative features of the OVRO beam (Figure 3c). Based on Figure 7, the possibility that the positive bias in Figure 6a is due to extended cloud emission is unlikely because the average image is centered and is clearly point-like (whereas we would expect cloud emission to be extended and randomly distributed). Thus we conclude that the positive bias observed in Figures 6a and 7 probably represents underlying weak mm-wavelength emission from point sources, and that the mean flux for the ensemble is  $0.32 \pm 0.06$  mJy.

## 5. Circumstellar Masses

The  $\lambda 3\text{mm}$  continuum sources listed in Table 1 represent thermal dust emission, as opposed to optically-thin free-free emission from hot plasma, because the  $\nu^{-0.1}$  frequency



dependence of free-free emission would imply higher fluxes in cm-wavelength VLA images from Gaume et al. (1992) than were actually observed. These authors imaged NGC 2024 at  $\lambda 1.3\text{cm}$  with an RMS noise level of  $\sim 0.6$  mJy, and detected emission only from IRS 2, NCP, and SCP. For the weakest object in Table 1, which has a  $\lambda 3\text{mm}$  flux of 4.23 mJy, the implied  $\lambda 1.3\text{cm}$  flux for optically-thin free-free emission would be 4.90 mJy, easily detectable in the Gaume et al. (1992) image. In addition, although IRS 2 is detected in the  $\lambda 1.3\text{cm}$  image with  $S_\nu = 19$  mJy, the measured  $\lambda 3\text{mm}$  flux of 111.17 mJy is much higher than that predicted for optically-thin free-free emission, indicating that at least some of the  $\lambda 3\text{mm}$  emission is due to dust.

The mass of circumstellar material (dust + gas, assuming a standard ISM gas to dust ratio) can be estimated from the observed flux in the OVRO  $\lambda 3\text{mm}$  continuum image following Hildebrand (1983):

$$M_{\text{circumstellar}} = \frac{S_\nu d^2}{\kappa_\nu B_\nu(T_{\text{dust}})}. \quad (1)$$

Here,  $\nu$  is the observed frequency,  $S_\nu$  is the observed flux,  $d$  is the distance to the source,  $\kappa_\nu = \kappa_0(\nu/\nu_0)^\beta$  is the mass opacity,  $T_{\text{dust}}$  is the dust temperature, and  $B_\nu$  is the Planck function. We assume  $d = 415$  pc (Anthony-Twarog 1982),  $\kappa_0 = 0.02 \text{ cm}^2 \text{ g}^{-1}$  at  $1300 \mu\text{m}$ ,  $\beta = 1.0$  (Hildebrand 1983; Beckwith et al. 1990), and  $T_{\text{dust}} = 20$  K (see discussion in Carpenter 2002). Uncertainties in the assumed values of these parameters (notably  $\kappa$ ) imply that the derived masses are uncertain (in an absolute sense) by at least a factor of 3 (e.g., Pollack et al. 1994). For the sources detected in our mosaic, we derive circumstellar masses ranging from 0.07 to  $1.71 M_\odot$ . The  $5\sigma$  mass detection limit is  $\sim 0.06 M_\odot$ , although this limit varies by  $\sim 20\%$  across the mosaic.

The OVRO observations alone do not have the angular resolution or kinematic information necessary to determine whether the circumstellar material is distributed in circumstellar disks or envelopes, or combinations of the two. If any of our  $\lambda 3\text{mm}$  continuum sources are also detected in the infrared, the observed mm-wavelength dust emission probably arises in flattened distributions since, for spherical distributions of material the columns of dust implied by the mm-wavelength flux would completely block out any near-IR emission (see, e.g., Beckwith et al. 1990). For even the weakest source in Table 1, the implied extinction for a spherical mass distribution would exceed 300 magnitudes. In contrast, de-reddening the sources in Figure 1 to the 0.3 Myr isochrone yields extinction estimates of  $\lesssim 50$  magnitudes for the infrared sources in NGC 2024. Therefore, the millimeter emission detected towards any K-band sources probably originates from flattened spatial distributions, probably disks, and not from envelopes of gas and dust.

NGC 2024 contains 147 K-band detected cluster members and 10 mm continuum sources

within the unit gain region of our OVRO mosaic. As discussed in §4, one of the mm sources corresponds to the K-band source IRS 2, an early B-type star where the dust temperature could be substantially hotter than the 20 K used in Equation 1. Since this would lead to a correspondingly lower circumstellar dust mass, the visual extinction argument presented above does not necessarily apply, and we cannot rule out circumstellar envelope emission for IRS 2. Since the main goal of this study is to determine the frequency of disk masses around low mass stars, we exclude IRS 2, and by the same argument, we also exclude IRS 1 and IRS 2b from our analysis (Garrison 1968; Bik et al. 2003). We also exclude two K-band sources that correspond spatially with mm emission from NCP and a negative sidelobe artifact (§4).

Of the remaining sample of 151 low-mass objects within the unit gain contour (9 mm and 142 near-IR), the mm sources FIR 2 and FIR 4 are tentatively associated with K-band cluster members (§4), leaving 149 unique sources. Since the associations of K-band sources with FIR 2 and 4 are tentative, the quoted fraction of near-infrared sources with disks should be considered an upper limit. None of the remaining 140 K-band sources within the OVRO mosaic, which most likely have stellar masses  $\lesssim 1\text{--}2\text{ M}_\odot$  (see Figure 1), have been detected in the  $\lambda 3\text{mm}$  continuum at the locally-determined  $3\sigma$  noise level or greater. Therefore, the fraction of low-mass K-band cluster members in NGC 2024 with a disk mass  $\gtrsim 0.035\text{ M}_\odot$  is at most 1.4%. However, millimeter emission has been detected for the *ensemble* of K-band sources with a mean flux of  $0.32 \pm 0.06\text{ mJy}$  (§4; Figures 6 and 7). Since the emission is compact, and centered on the K-band sources, we suggest that the mm-wavelength emission originates in disks. Using the assumptions in Equation 1, this mean flux implies an average circumstellar disk mass for the ensemble of low-mass near-IR cluster members of  $0.005 \pm 0.001\text{ M}_\odot$ .

## 6. Discussion

Excluding the massive stars (see §5), the frequency of circumstellar masses (in disks and/or envelopes) greater than  $0.06\text{ M}_\odot$  in NGC 2024 is  $\sim 6\%$  (9/151). Although K-L color excesses for NGC 2024 cluster members suggest that  $86 \pm 8\%$  of the stars have circumstellar disks (Haisch et al. 2000), these two estimates of the disk fraction are not necessarily contradictory, since the near-IR emission probes trace material ( $\sim 10^{-6}\text{ M}_\odot$ ) within  $\sim 0.1\text{ AU}$  of the star, while millimeter emission traces massive ( $\gtrsim 0.035\text{ M}_\odot$ ) outer circumstellar material.

We compare our results for NGC 2024 with an analogous  $\lambda 3\text{mm}$  continuum survey of IC 348 (Carpenter 2002). Although the IC 348 survey contains shorter uv spacings than the NGC 2024 mosaic, and samples  $\sim 2$  times larger spatial scales, this does not affect the

comparison since no emission (compact or extended) was detected in IC 348. NGC 2024 and IC 348 are similar in that each cluster contains on the order of 300 stars (Lada et al. 1991; Herbig 1998), the spectral types of the most massive stars are comparable ( $\sim$ O8 for NGC 2024, B0 for IC 348), and the stellar mass distributions are consistent with a Miller-Scalo IMF (Meyer 1996; Luhman et al. 1998). The primary difference between the two clusters is that NGC 2024 is more deeply embedded within the molecular cloud and younger than IC 348 (see §2). No  $\lambda$ 3mm continuum sources were detected in IC 348 with a  $3\sigma$  upper limit of  $0.025 M_{\odot}$  out of a sample of 95 known infrared cluster members. In contrast,  $\sim 6\%$  of cluster members in NGC 2024 are surrounded by more than  $0.06 M_{\odot}$  of material (which could be distributed in disks, envelopes, or combinations of the two). Using the Fisher Exact Test, the probability that these two measurements are drawn from the same distribution is 1.5%. Moreover, the average disk mass for the ensemble of low-mass stars in NGC 2024 is  $0.005 \pm 0.001 M_{\odot}$ , compared to  $0.002 \pm 0.001 M_{\odot}$  in IC 348. Assuming that the differences between NGC 2024 and IC 348 are due to temporal evolution, these observations indicate that massive disks/envelopes dissipate on timescale  $\lesssim 2$  Myr, and that the average disk mass decreases by a factor of  $2.5 \pm 1.3$  between  $\sim 0.3$  and 2 Myr <sup>1</sup>.

The NGC 2024 results can also be compared with the disk masses in the Orion Nebula cluster, which have been computed from both  $\lambda$ 3.5mm (Mundy et al. 1995) and  $\lambda$ 1.3mm continuum observations (Bally et al. 1998). At  $\lambda$ 3.5mm, a  $3\sigma$  upper limit of 5.7 mJy was derived for the flux observed above the level of the expected free-free emission for a sample of 33 proplyds in the Orion Nebula cluster. Using Equation 1 with the same assumptions as in §5, this translates into a  $3\sigma$  upper limit on disk mass of  $0.17 M_{\odot}$ . An upper limit on the *average* disk mass for these 33 sources is  $0.03 M_{\odot}$ . The  $\lambda$ 1.3mm results yield a  $3\sigma$  upper limit of  $0.047 M_{\odot}$  for five proplyd sources. The lack of massive disks in the Orion Nebula cluster is similar to the results for NGC 2024 and IC 348.

In contrast to NGC 2024, IC 348, and the Orion Nebula cluster, a large fraction of the stars in Taurus show evidence for massive circumstellar disks. We have compiled a sample of 164 stars in Taurus that have been observed at millimeter wavelengths, including sources observed by Beckwith et al. (1990), Osterloh & Beckwith (1995), and Motte & André (2001). All detected sources included in the sample are  $\geq 90\%$  concentrated within the  $\sim 11''$  beams of the various surveys. We also compiled K-band magnitudes for the sample, either from the literature or from 2MASS. Approximately 21% of the sample sources show evidence for circumstellar disks with masses  $\gtrsim 0.01 M_{\odot}$ .

---

<sup>1</sup>Another possible explanation for the higher observed flux in NGC 2024 relative to IC 348 is that one or more of the assumed quantities in Equation 1 (e.g., temperature or opacity) is different in the two regions. Regardless of the underlying factors, our measurement suggests disk evolution between  $\sim 0.3$  and 2 Myr.

In NGC 2024,  $\sim 6\%$  of cluster members have circumstellar masses greater than  $\sim 0.06 M_{\odot}$ . In Taurus, the percentage of sources with  $> 0.06 M_{\odot}$  of circumstellar material is  $\sim 3\%$ , and the probability that the two samples are drawn from the same distribution is  $75.9\%$ . Based on these results, we cannot statistically distinguish between the frequencies of sources with circumstellar masses  $> 0.06 M_{\odot}$  in NGC 2024 and Taurus. However, if we compare the observed mm fluxes for only low-mass K-band sources, where the millimeter emission likely originates in circumstellar disks, we find a possible difference. The fraction of near-IR cluster members in NGC 2024 with circumstellar disks  $\gtrsim 0.035 M_{\odot}$  is  $\leq 1.4\%$ . In contrast,  $\sim 5\%$  of objects in Taurus have circumstellar disks  $> 0.035 M_{\odot}$ . Follow-up observations of the Taurus sources at high angular resolution show that the dust usually lies in compact flattened distributions, and not in massive envelopes (e.g., Dutrey et al. 1996; Looney et al. 2000). Moreover, these objects are quite bright at K-band, and if placed at the distance of NGC 2024, would be detectable in the UKIRT K-band image for visual extinctions  $< 50$  mag. Thus, despite the fact that NGC 2024 is younger than Taurus, the fraction of K-band sources with massive disks is lower. The probability that the frequencies of massive disks around K-band sources in Taurus and NGC 2024 are drawn from the same distribution is  $\leq 8.5\%$ .

In summary, the NGC 2024 and IC 348 clusters combined contain at most 2 K-band sources out of a total of 239 observed, or  $\leq 0.8\%$ , that are associated with millimeter continuum emission characteristic of massive circumstellar disks ( $M > 0.035 M_{\odot}$ ). In comparison,  $5\%$  of the sources in Taurus contain such disks. These combined results suggest that the rich cluster environments may not be conducive to forming large, massive circumstellar disks. Scally & Clarke (2001) showed that massive disks in rich clusters may be inhibited by photoevaporation or tidal disruption due to close encounters with massive stars, with photoevaporation as the dominant effect. Although the ionizing flux from the massive stars in NGC 2024 will be highly attenuated by the extinction in the dense core, these effects may help to explain the lack of massive disks.

The derived upper limits on circumstellar disk masses in NGC 2024 and IC 348 can be compared with the minimum mass needed to form a system like our own Solar System. Summing the mass contained in Solar planets, and assuming a standard ISM gas to dust ratio, the minimum mass of the proto-solar nebula is  $\sim 0.01 M_{\odot}$  (Weidenschilling 1977; Hayashi 1981). This reflects primarily the matter needed to form Jupiter. The true mass of the proto-solar nebula may have been higher than this minimum estimate, depending on the efficiency of conversion of proto-solar dust and gas into planets. The average disk mass determined for K-band sources in NGC 2024,  $0.005 \pm 0.001 M_{\odot}$ , is comparable to the expected mass of the proto-solar nebula. Although uncertainties in the assumed values of the parameters used in Equation 1 imply that the derived masses are uncertain by at least a factor of 3, our data indicate that the average star in NGC 2024 possesses a disk massive

enough to form a planet with  $M \lesssim M_{\text{Jupiter}}$ .

In contrast, the  $3\sigma$  upper limits on disk mass in both NGC 2024 and IC 348 rule out the existence of disks massive enough to form planets with several Jupiter masses. Our results therefore imply either that the formation of massive planets (i.e., several Jupiter masses) is relatively rare in NGC 2024 and IC 348, or that the aggregation of dust grains into planetesimals (and eventually planets) has already occurred within  $\sim 1$  Myr, depleting the disks of small grains that OVRO would see in emission. The timescale for giant planet formation via core accretion is thought to be  $\sim 10^6 - 10^8$  years (e.g., Pollack et al. 1996), and thus it is unlikely that planets of several Jupiter masses have formed by this method around most of the stars in NGC 2024 (which has an age of  $\sim 3 \times 10^5$  years). A possible implication of this might be that giant planets do not form in rich clusters. A recent survey of the 47 Tuc cluster failed to detect any planets (where they expected to find  $\sim 17$ ; Gilliland et al. 2000), providing some support for this possibility. An alternative explanation is that the core accretion model for giant planet formation is not operating in NGC 2024. Giant planet formation through gravitational instabilities in circumstellar disks requires only  $\sim 10^3 - 10^5$  years (e.g., Boss 1998), and might provide a viable explanation for quick massive planet formation in NGC 2024.

## 7. Conclusions

We have imaged the central  $2'.5 \times 2'.5$  region of NGC 2024 in  $\lambda 3\text{mm}$  continuum emission with the OVRO millimeter-wavelength interferometer. The mosaic encompasses 147 K-band detected cluster members and the molecular ridge seen previously in dust continuum emission. We detected 10 point sources within the unit gain region of the OVRO mosaic above the  $5\sigma$  level (where  $\sigma \sim 0.75$  Jy). One of the millimeter sources is coincident with the early B-type star IRS 2. Two other millimeter sources, FIR 2 and FIR 4, are near to but not exactly coincident with infrared cluster members. No millimeter emission was detected towards the other low-mass infrared cluster members above the  $3\sigma$  level of 2.25 mJy. The mean  $\lambda 3\text{mm}$  flux toward the ensemble of K-band sources is  $0.32 \pm 0.06$  mJy.

We use the  $\lambda 3\text{mm}$  fluxes to estimate the circumstellar dust masses assuming that the millimeter-wavelength emission is optically thin, with a temperature of 20 K, and adopting a mass opacity coefficient of  $\kappa = 0.02 \text{ cm}^2 \text{ g}^{-1}$  at 1.3 mm. With these assumptions, the circumstellar mass (dust plus gas) ranges from 0.07 to  $1.71 M_{\odot}$  for the 10 detected sources. The  $3\sigma$  upper limit to the circumstellar mass around the individual K-band sources (excluding the tentative associations with FIR 2 and FIR 4) is  $\sim 0.035 M_{\odot}$ , and the average mass for the ensemble of low-mass K-band sources is  $0.005 \pm 0.001 M_{\odot}$ . These results show that

at the age of the NGC 2024 cluster ( $\sim 0.3$  Myr; Meyer 1996),  $\sim 6\%$  of cluster members have massive ( $\gtrsim 0.06 M_{\odot}$ ) circumstellar structures (disks and/or envelopes), and many of the sources may possess low-mass circumstellar disks.

We compare our results to a similar millimeter continuum survey of IC 348 (Carpenter 2002). None of the 95 cluster members observed in IC 348 were detected in the millimeter continuum above the  $3\sigma$  level of  $0.025 M_{\odot}$  in IC 348. In contrast, we detect more than  $\sim 0.06 M_{\odot}$  of circumstellar material around  $\sim 6\%$  of cluster members in NGC 2024. Moreover, the average disk mass around a typical low-mass K-band source in NGC 2024 is  $2.5 \pm 1.3$  times higher than in IC 348. Thus, there may be some evolution of circumstellar disks and/or envelopes on  $\sim 1$  Myr timescales.

The fraction of circumstellar disks more massive than  $\sim 0.035 M_{\odot}$  around near-IR cluster members is at most  $0.8\%$  in NGC 2024 and IC 348 combined, suggesting that massive disks are either very rare, or non-existent, in rich cluster environments. In contrast,  $\sim 5\%$  of the sources in Taurus have circumstellar disks more massive than  $0.035 M_{\odot}$ , even though Taurus is older than, or of similar age to, the rich clusters. This may imply different physical mechanisms for disk formation and evolution in clustered versus isolated star forming regions.

The average disk mass of  $\sim 0.005 M_{\odot}$  for the ensemble of K-band sources is comparable to the minimum mass of material necessary to form the proto-solar nebula, which implies that many objects in NGC 2024 possess disks massive enough to form planets with the approximate mass of Jupiter. However, the  $3\sigma$  limit of  $0.035 M_{\odot}$  on the masses of circumstellar disks in NGC 2024 suggests that high-mass planets (several Jupiter masses) may have either already formed (thus depleting the disks of small grains), or may never form in this cluster.

**Acknowledgments.** JAE is supported by a Michelson Graduate Research Fellowship. JMC acknowledges support from Long Term Space Astrophysics Grant NAG5-8217 and the Owens Valley Radio Observatory, which is supported by the National Science Foundation through grant AST-9981546. This publication makes use of data products from the Two Micron All Sky Survey, which is a joint project of the University of Massachusetts and the Infrared Processing and Analysis Center, funded by the National Aeronautics and Space Administration and the National Science Foundation. 2MASS science data and information services were provided by the Infrared Science Archive (IRSA) at IPAC.

## REFERENCES

- Ali, B. 1996, Ph.D. Thesis, The Ohio State University
- André, P. & Montmerle, T. 1994, *Ap. J.*, 420, 837

- Anthony-Twarog, B.J. 1982, AJ, 87, 1213
- Bally, J., Testi, L., Sargent, A., & Carlstrom, J. 1998, AJ, 116, 854
- Barnes, P.J., Crutcher, R.M., Bieging, J.H., Storey, J.W.V., & Willner, S.P. 1989, Ap. J., 342, 883
- Beckwith, S.V.W., Sargent, A.I., Chini, R.S., & Guesten, R. 1990, AJ, 99, 924
- Bik, A., Lenorzer, A., Kaper, L., Comerón, F., Waters, L.B.F.M., de Koter, A., & Hanson, M.M. 2003, A&A, , in press
- Boss, A.P. 1998, Ap. J., 503, 923
- Brown, A.G.A., de Geus, E.J., & de Zeeuw, P.T. 1994, A&A, 289, 101
- Carpenter, J.M. 2002, AJ, 124, 1593
- Carpenter, J.M. 2000, AJ, 120, 3139
- Chandler, C.J., & Carlstrom, J.E. 1996, Ap. J., 466, 338
- Cohen, J.G., Frogel, J.A., Perrson, S.E., & Elias, J.H. 1981, Ap. J., 249, 481
- Crutcher, R., Henkel, C., Wilson, T.L., Johnston, K., Bieging, J. 1986, Ap. J., 307, 302
- D’Antona, F. & Mazzitelli, I. 1997, Memorie della Societa Astronomica Italiana, 68, 807
- D’Antona, F., & Mazzitelli, I. 1994, ApJS, 90, 467
- Dutrey, A., Guilloteau, S., Duvert, G., Prato, L., Simon, M., Schuster, K., & Menard, F. 1996, A&A, 309, 493
- Garrison, R.F. 1968, PASP, 80, 20
- Gaume, R.A., Johnston, K.J., & Wilson, T.L. 1992, Ap. J., 388, 489
- Gilliland, R.L., et al. 2000, Ap. J., 545, L47
- Grasdalen, G.L. 1974, Ap. J., 193, 373
- Haisch, K.E., Lada, E.A., & Lada, C.J. 2001, AJ, 121, 2065
- Haisch, K.E., Lada, E.A., & Lada, C.J. 2000, AJ, 120, 1396
- Hayashi, C. 1981, Prog. Theor. Phys. Supp. 1981, 70, 35

- Henning, T., Pfau, W., Zinnecker, H., & Prusti, T. 1993, *A&A*, 276, 129
- Herbig, G.H. 1998, *Ap. J.*, 497, 736
- Hildebrand, R.H. 1983, *QJRAS*, 24, 267
- Hillenbrand, L.A., Meyer, M.R., & Carpenter, J.M. 2003, in preparation.
- Hillenbrand, L.A. 1997, *AJ*, 113, 1733
- Hogerheijde, M.R., Jayawardhana, R.J., Johnstone, D., Blake, G.A., & Kessler, J.E. 2002, *AJ*, 124, 3387
- Itoh, Y., et al. 2003, *Ap. J.*, 586, L141
- Jiang, D.R., Perrier, C., & Léna, P. 1984, *A&A*, 135, 249
- Koerner, D.W., & Sargent, A.I. 1995, *AJ*, 109, 2138
- Lada, C.J., Muench, A.A., Haisch, K.E., Jr., Lada, E.A., Alves, J.F., Tollestrup, E.V., & Willner, S.P. 2000, *AJ*, 120, 3162
- Lada, E.A., Strom, K.M., & Meyers, P.C. 1993, in *Protostars and Planets III*, ed. E.H. Levy & J.I. Lunine (Tucson: Univ. of Arizona Press), 245
- Lada, E.A. 1999, in *The Origin of Stars and Planetary Systems*, ed. C.J. Lada & N. Kylafis (Dordrecht: Kluwer), 441
- Lada, E.A., Evans, N.J. II, Depoy, D., & Gatley, I. 1991, *Ap. J.*, 371, 171
- Looney, L. W., Mundy, L. G., & Welch, W. J. 2000, *Ap. J.*, 529, 477
- Luhman, K.L., Rieke, G.H., Lada, C.J., & Lada, E.A. 1998, *Ap. J.*, 508, 347
- Luhman, K.L. 1999, *Ap. J.*, 525, 466
- Meyer, M.R. 1996, Ph.D. Thesis, University of Massachusetts Amherst
- Mezger, P.G., Sievers, A.W., Haslam, C.G.T., Kreysa, E., Lemke, R., Mauersberger, R., & Wilson, T.L. 1992, *A&A*, 256, 631
- Mezger, P.G., Chini, R., Kreysa, E., Wink, J.E., & Salter, C.J. 1988, *A&A*, 191, 44
- Moore, T.J.T., Chandler, C.J., Gear, W.K., & Mountain, C.M. 1989, *M.N.R.A.S.*, 237, 1P
- Motte, F. & André, P. 2001, *A&A*, 365, 440



- Motte, F., André, P., & Neri, R. 1998, *A&A*, 336, 150
- Mundy, L.G., Looney, L.W., & Lada, E.A. 1995, *Ap. J. (Letters)*, 452, L137
- Nuernberger, D., Brandner, W., Yorke, H.W., & Zinnecker, H. 1998, *A&A*, 330, 549
- Nuernberger, D., Chini, R., & Zinnecker, H. 1997, *A&A*, 324, 1036
- O’Dell, C.R., & Wong, S.K. 1996, *AJ*, 111, 846
- Osterloh, M. & Beckwith, S.V.W. 1995, *Ap. J.*, 439, 288
- Padgett, D.L., Brandner, W., Stapelfeldt, K.R., Strom, S.E., Terebey, S., & Koerner, D. 1999, *AJ*, 117, 1490
- Pollack, J.B., Hubickyj, O., Bodenheimer, P., Lissauer, J.J., Podolak, M., & Greenzweig, Y. 1996, *Icarus*, 124, 62
- Pollack, J. B., Hollenbach, D., Beckwith, S., Simonelli, D. P., Roush, T., & Fong, W. 1994, *Ap. J.*, 421, 615
- Richer, J.S., Hills, R.E., Padman, R., & Russell, A.P.G. 1989, *M.N.R.A.S.*, 241, 231
- Sault, R.J., Teuben, P.J., & Wright, M.C.H. 1995, *ASP Conf. Ser.* 77, 433
- Scally, A., & Clarke, C. 2001, *M.N.R.A.S.*, 325, 449
- Scoville, N.Z., Carlstrom, J.E., Chandler, C.J., Phillips, J.A., Scott, S.L., Tilanus, R.P.J., & Wang, Z. 1993, *PASP*, 105, 1482
- Strom, K.E., Strom, S.E., Edwards, S., Cabrit, S., & Skrutskie, M.F. 1989, *AJ*, 97, 1451
- Strom, S.E., Edwards, S., & Skrutskie, M.F. 1993, in *Protostars and Planets III*, ed. E.H. Levy & J.I. Lunine (Tucson: Univ. Arizona Press), 837
- Testi, L., & Sargent, A.I. 1998, *AJ*, 116, 854
- Weidenschilling, S.J. 1977, *Ap&SS*, 51, 153
- Wilson, T.L., Mehringer, D.M., & Dickel, H.R. 1995, *A&A*, 303, 840

Table 1. Sources detected in  $\lambda$ 3mm continuum with OVRO

ID	Source Name	$\alpha$ (J2000)	$\delta$ (J2000)	FWHM	PA ( $^\circ$ )	$S_\nu$ (mJy) <sup>a</sup>	$M_{\text{circumstellar}}$ ( $M_\odot$ )	
1	FIR 2	05 41 42.59	-01 54 9.21	$3''.43 \times 2''.39$	-49.5	$5.07 \pm 0.76$	0.08	
2	...	05 41 42.83	-01 54 14.48			$6.19 \pm 0.76$	0.10	
3	FIR 3	05 41 43.11	-01 54 26.15	$3''.63 \times 2''.26$	-34.5	$34.22 \pm 0.93$	0.53	
4	FIR 4	05 41 44.13	-01 54 45.58	$2''.10 \times 2''.80$	-143.1	$15.41 \pm 0.86$	0.24	
5	...	05 41 44.23	-01 55 2.72	$2''.42 \times 1''.91$	-0.5	$4.26 \pm 0.73$	0.07	*
6	...	05 41 44.67	-01 55 1.83			$4.82 \pm 0.73$	0.07	*
7	...	05 41 45.04	-01 55 4.33	$3''.23 \times 2''.41$	-20.9	$4.23 \pm 0.73$	0.07	
8	...	05 41 45.41	-01 54 26.39	$2''.54 \times 2''.35$	24.8	$15.23 \pm 1.10$	0.24	
9	IRS 2	05 41 45.80	-01 54 29.71	$1''.94 \times 2''.17$	36.5	$111.17 \pm 1.10$	1.71	
10	...	05 41 45.83	-01 53 49.37	$2''.25 \times 2''.88$	5.9	$5.93 \pm 0.88$	0.09	
11	FIR 5	05 41 44.33	-01 55 40.98	$2''.79 \times 2''.47$	-164.5	$81.97 \pm 0.87$	1.27	†
12	...	05 41 44.48	-01 55 41.33			$16.67 \pm 0.87$	0.27	†
13	FIR 6	05 41 45.14	-01 56 4.22	$2''.54 \times 2''.06$	-40.1	$58.55 \pm 1.32$	0.90	†

References. — †—These sources lie outside of the unit gain contour, and have been scaled by the inverse gain;  
 \*—These sources are probably artifacts due to imperfect cleaning of extended emission; <sup>a</sup>—Uncertainties are  $1\sigma$ ,  
 where  $\sigma$  is the locally-determined RMS. .

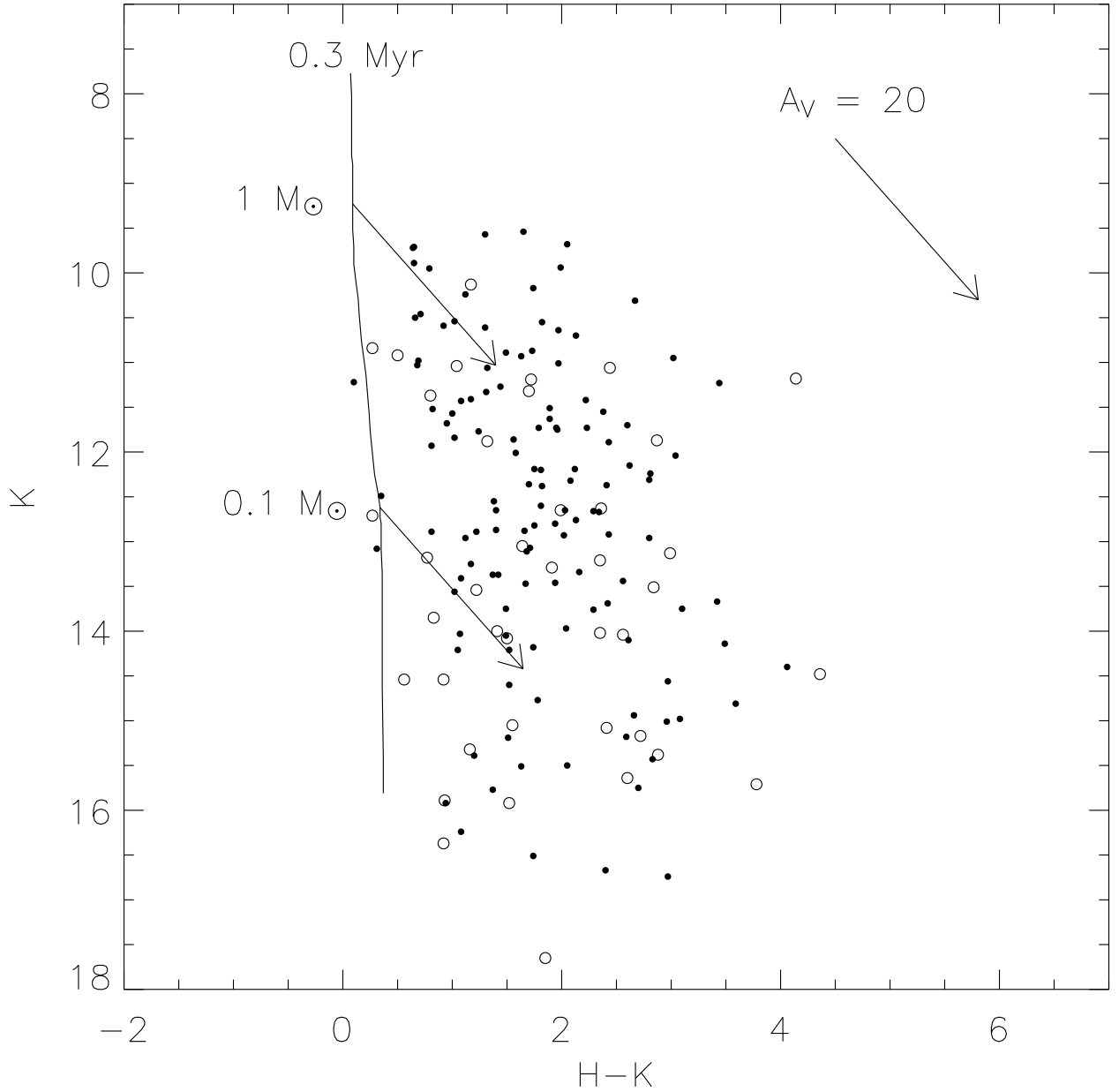


Fig. 1.— Color-magnitude diagram for the stars in the NGC 2024 cluster (based on data from Meyer 1996). We also plot the isochrone for stars of age 0.3 Myr (D’Antona & Mazzitelli 1997), and the extinction vectors (Cohen et al. 1981) for a  $1 M_{\odot}$  star and a  $0.1 M_{\odot}$  star, assuming  $A_V = 20$ . Sources that lie within the unit gain contour of our OVRO mosaic (see Figure 2) are indicated by filled circles, while open circles represent cluster members that lie outside of the unit gain region.

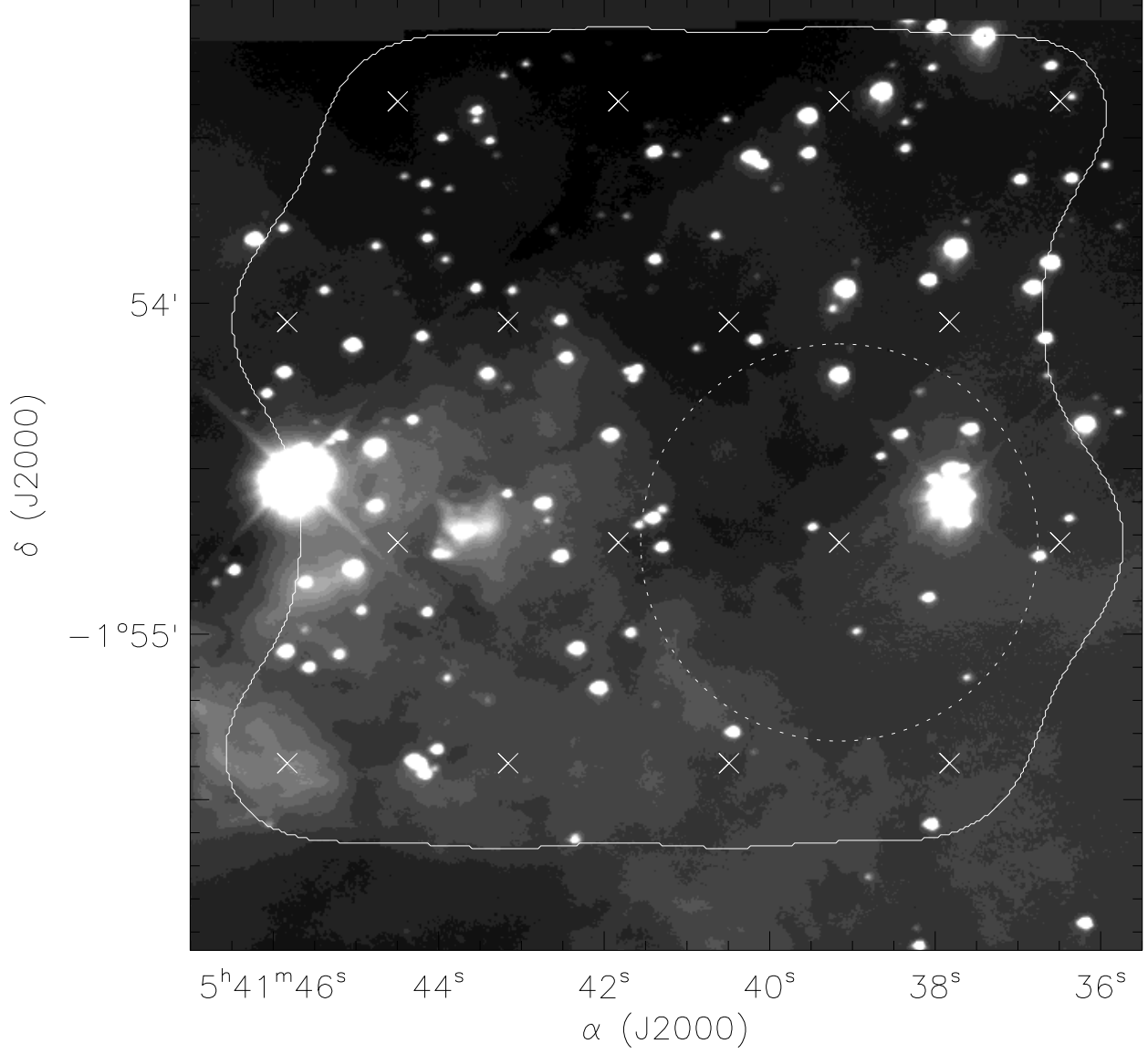


Fig. 2.— Pointing positions for the OVRO mosaic (“X” symbols), plotted over a K-band image of the NGC 2024 cluster from Meyer (1996). The FWHM of the OVRO primary beam at the observed frequency (100 GHz) is indicated by the dotted circle in the lower-right corner, and the unit gain contour of the map is shown by the solid curve.

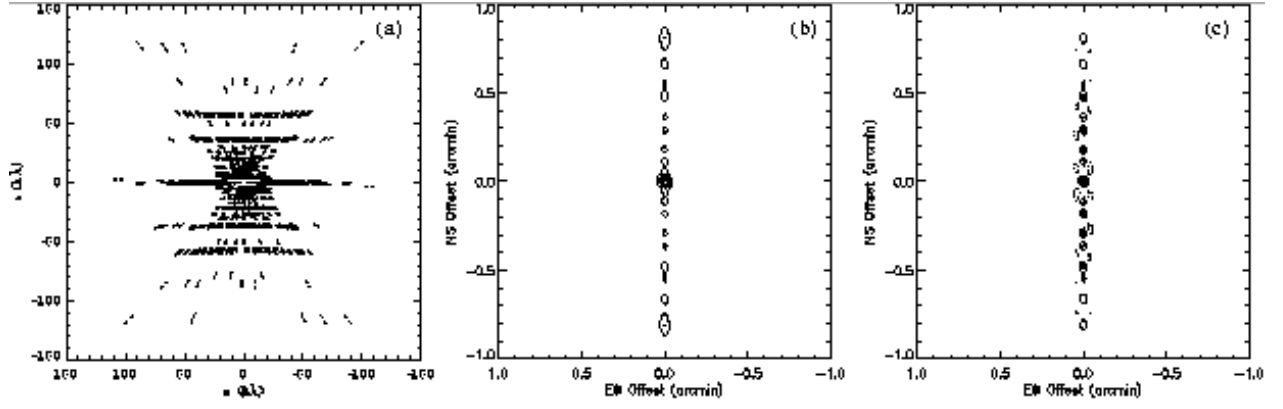


Fig. 3.— (a) uv coverage of the OVRO observations of NGC 2024. (b) Resultant beam after weighting the complete OVRO data set using a robust parameter of 0.5. (c) The OVRO beam for only uv spacings  $> 20 \text{ k}\lambda$ . The contour increments in panels (b) and (c) are 0.2, positive contours are indicated by solid lines, and negative contours are indicated by dotted lines.

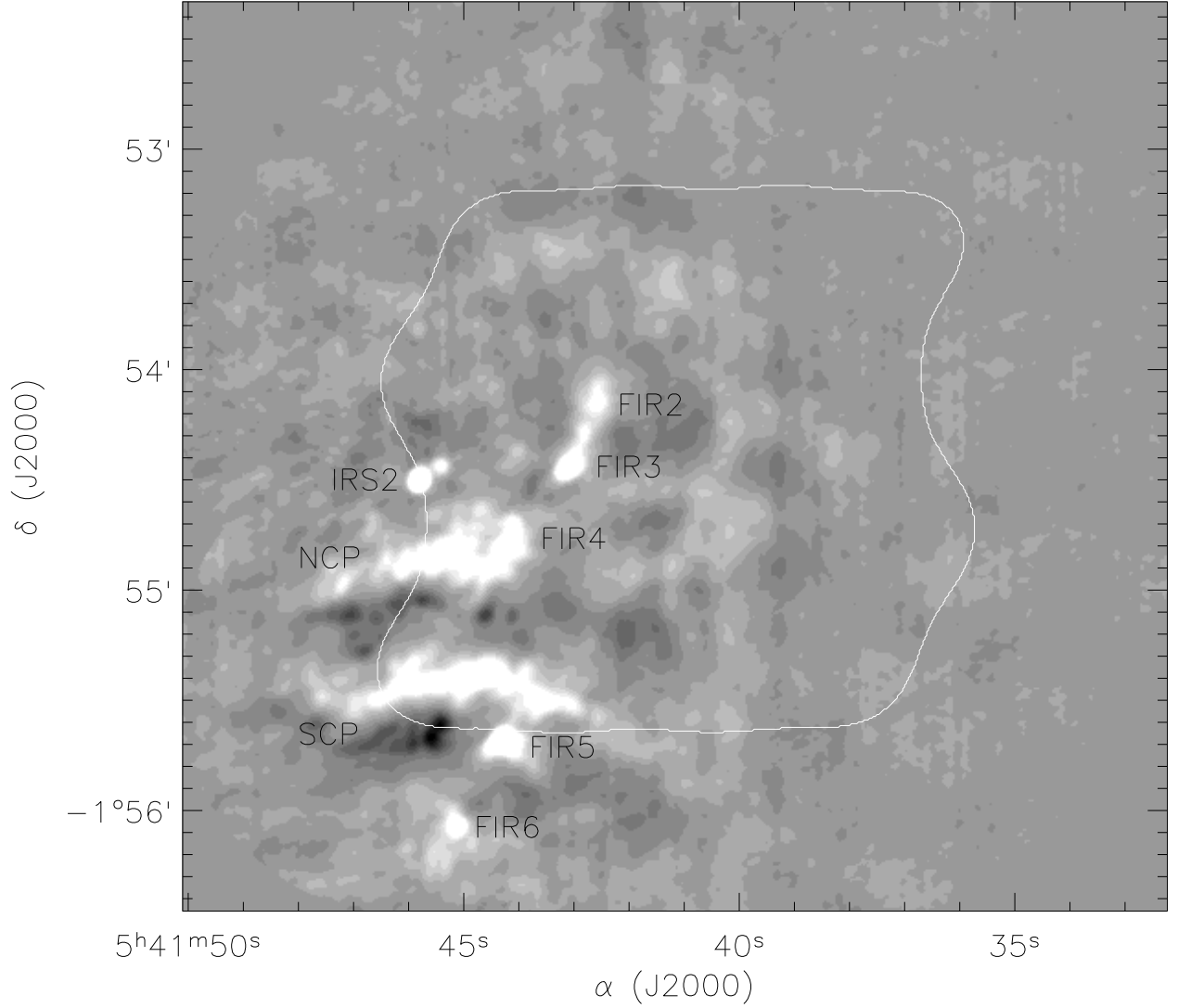


Fig. 4.— The NGC 2024 star forming region, imaged in  $\lambda 3\text{mm}$  continuum with the Owens Valley Millimeter Array (greyscale). All of the OVRO data were used to create this image, and the angular resolution is  $3''.84 \times 3''.22$ . The unit gain region of the mosaic encompasses a  $2'.5 \times 2'.5$  area, as indicated by the solid contour, and the average RMS of the residuals within the unit gain contour is  $\sim 1.3$  mJy. We have labeled the previously detected sub-mm sources FIR 2-6 (Mezger et al. 1988) and IRS 2 (Wilson et al. 1995). Also, the horizontal emission regions labeled NCP and SCP correspond spatially to the free-free emission regions observed in VLA centimeter continuum maps (Crutcher et al. 1986; Gaume et al. 1992). While it is difficult to distinguish FIR 4 from NCP in this image, FIR 4 is clearly visible in Figure 5.

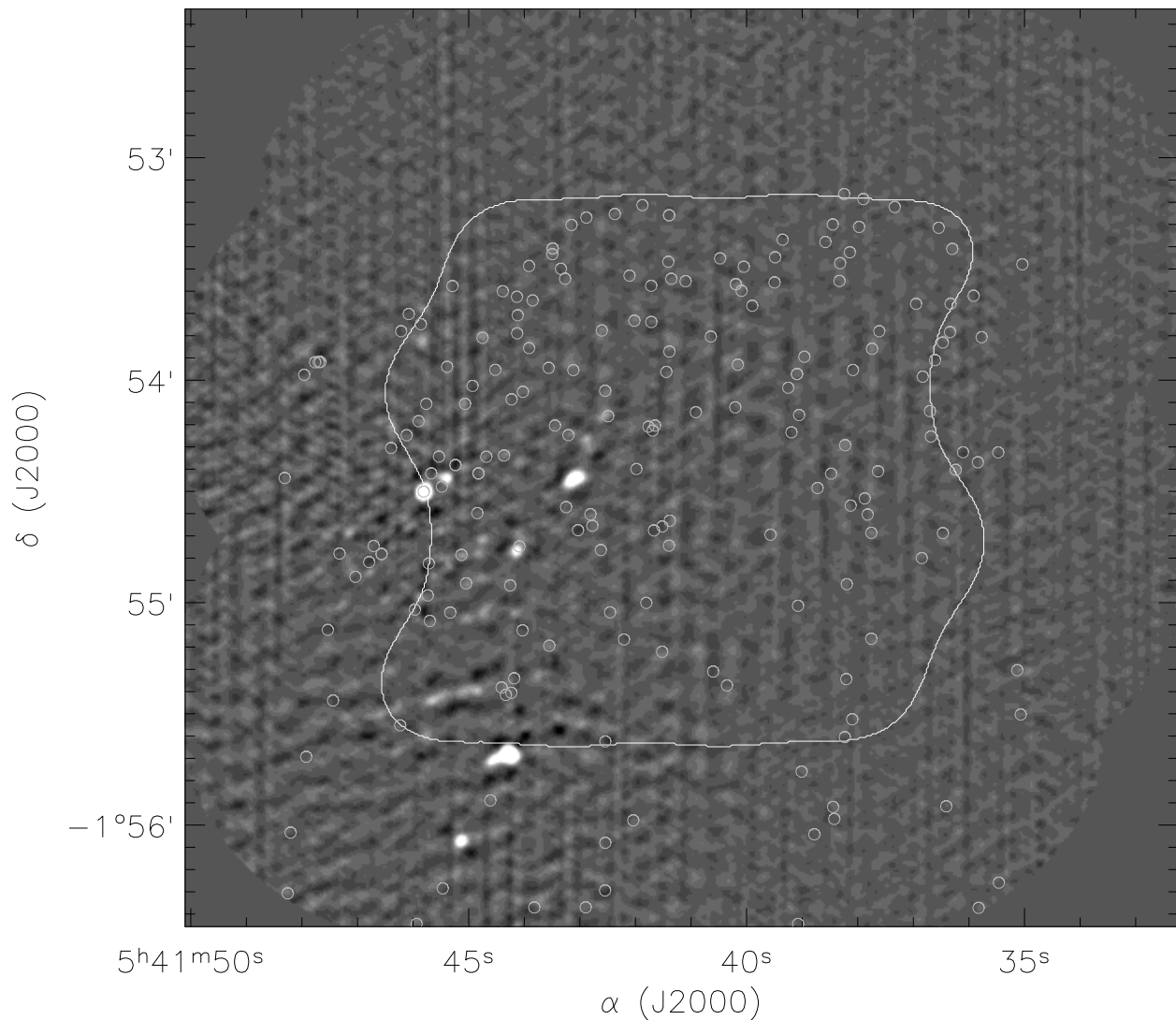


Fig. 5.— The NGC 2024 star forming region, imaged in  $\lambda 3\text{mm}$  continuum with the Owens Valley Millimeter Array (greyscale). This image is constructed from measurements with a uv radius  $> 20\text{ k}\lambda$ , and the resultant angular resolution is  $2''.53 \times 2''.13$ . The unit gain contour is indicated by a solid line, and the average RMS of the residuals within the unit gain contour is  $0.75\text{ mJy}$ . The positions of near-IR sources detected at K-band (Meyer 1996) are indicated with open circles.

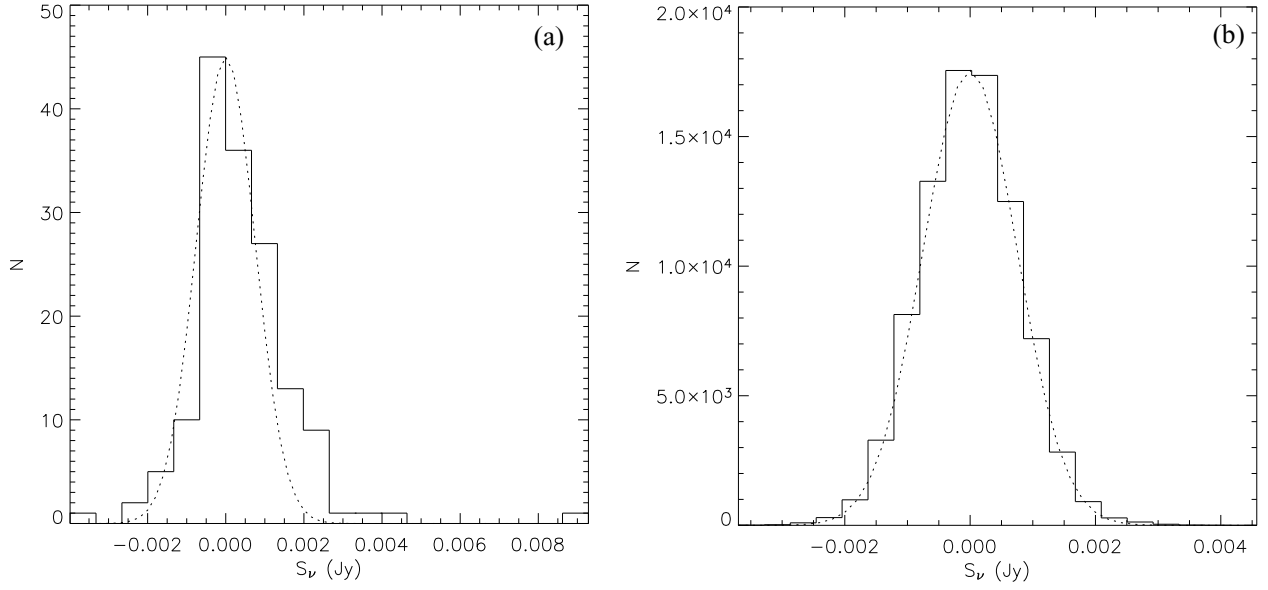


Fig. 6.— (a) Frequency distribution of  $\lambda 3\text{mm}$  continuum fluxes measured towards the low-mass NGC 2024 K-band cluster members within the unit gain contour of the OVRO mosaic (histogram). IRS 2 is off the scale of the plot at  $\sim 0.1$  Jy. The three sources with fluxes  $\gtrsim 2.5$  mJy correspond to slight offsets from FIR 2 and 4 (§4) and to part of the NCP structure. The extreme negative source with  $F \sim -4$  mJy is actually tracing a sidelobe artifact. (b) Frequency distribution of  $\lambda 3\text{mm}$  continuum fluxes for all pixels within the unit gain contour of the high-angular resolution OVRO map (Figure 5), where the bright ( $> 3.75$  mJy) point sources listed in Table 1 have been removed using CLEAN (histogram). In both panels, the frequency distribution expected for Gaussian noise with a mean of zero and an RMS of 0.75 mJy is indicated by a dotted line.



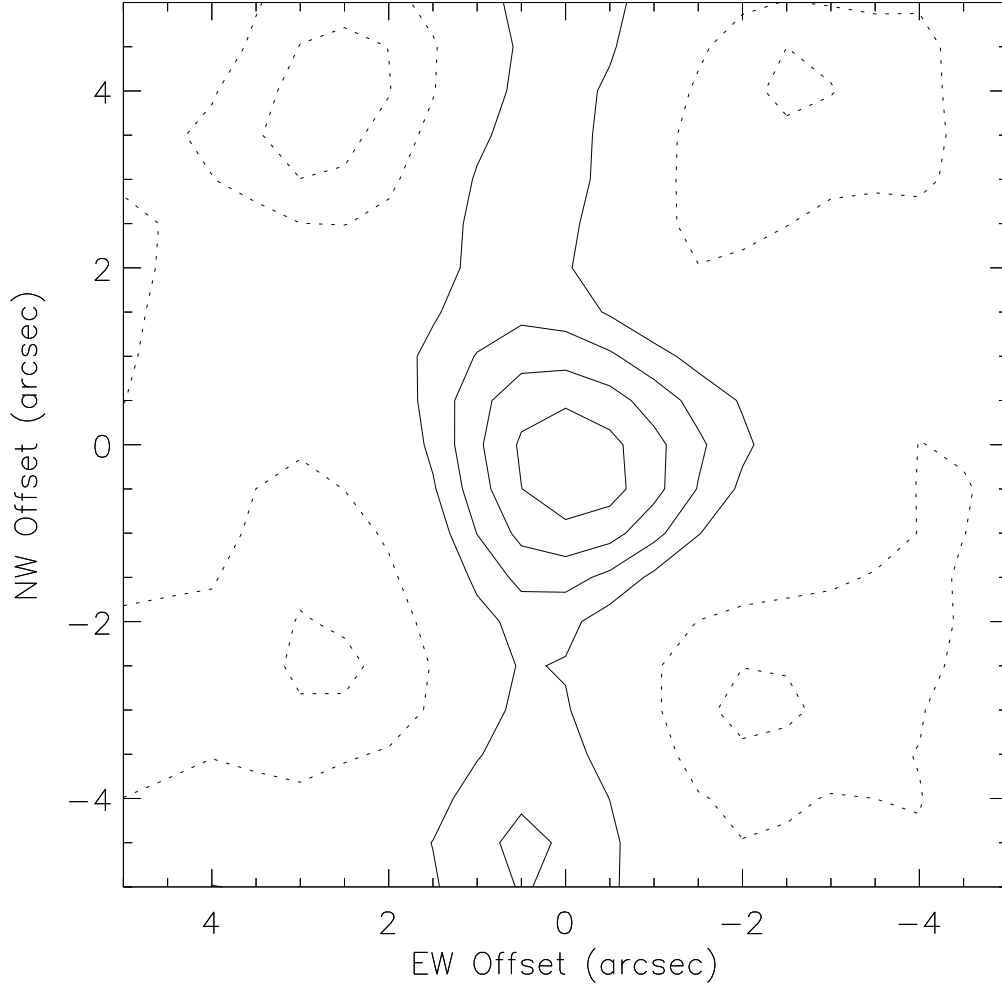


Fig. 7.— OVRO image created by averaging  $10'' \times 10''$  images towards the positions of known low-mass K-band cluster members in NGC 2024. The bright sources listed in Table 1 were removed using CLEAN before shifting and co-adding the images. The contour increment is given by the standard deviation of the mean for the flux distribution (0.06 mJy; §4). Negative contours are represented by dotted lines and positive contours are represented by solid lines. The FWHM of the emission, as well as the negative features, are consistent with the OVRO beam shown in Figure 3c. We also note that the emission is centered at (0,0), corresponding to the mean position of K-band sources. None of the individual stars used to create this image were detected at the  $\geq 3\sigma$  level, although the sources are detected in the mean at the  $\sim 5\sigma$  level. Assuming this compact emission originates from circumstellar disks, the average disk mass for the ensemble of K-band sources is  $\sim 0.005 M_{\odot}$ .